Soft Matter

PAPER

Cite this: Soft Matter, 2016, 12, 8919

Received 22nd August 2016, Accepted 1st October 2016

DOI: 10.1039/c6sm01928e

www.rsc.org/softmatter

Response of driven sessile drops with contact-line dissipation†

Joshua B. Bostwick*[a] and Paul H. Steen[b]

A partially-wetting sessile drop is driven by a sinusoidal pressure field that produces capillary waves on the liquid/gas interface. Response diagrams and phase shifts for the droplet, whose contact-line moves with contact-angle that is a smooth function of the contact line speed, are reported. Contact-line dissipation originating from the contact-line speed condition leads to damping for drops with finite contact-line mobility, even for inviscid fluids. The critical mobility and associated driving frequency to generate the largest contact-line dissipation is computed. Viscous dissipation is approximated using the irrotational flow and the critical Ohnesorge number bounding regions beyond which a given mode becomes over-damped is computed. Regions of modal coexistence where two modes can be simultaneously excited by a single forcing frequency are identified. Predictions compare favorably to related experiments on vibrated drops.

1 Introduction

Driven droplets play a critical role in a number of emerging technologies, such as 3D printing[1] with application to rapid prototyping,[2] self-cleansing surfaces for enhanced solar cell efficiency,[3] microfluidics,[4] inkjets,[5,6] spray cooling for high heat flux applications,[7] and drop atomization for drug delivery (aerosol) methods,[8] all of which involve the motion of liquids on scales where surface tension dominates.

Forcing of sessile drops can induce shape change or drive fluid transport. Shape change occurs in experiments by driving droplets using electrowetting,[9] surface acoustic waves,[10] air jets,[11] mechanically vibrated substrates[12,13] or pressure excitations.[14] Bulk translational motion of driven droplets can be achieved provided contact angle hysteresis can be overcome to mobilize the contact line.[15] Brunet *et al.*[16] have demonstrated that a mechanically-vibrated drop can be made to walk 'uphill' against gravity in a ratchet-like motion.[17] A description of the fluid mechanical droplet response to the applied driving force is crucial in understanding the aforementioned applications, as well as guiding future studies led by prediction. In this paper, we analyze the driven sessile drop by introducing external forcing through the drop's bulk pressure $p = F_0 e^{i\Omega t}$ with Ω the applied forcing frequency, as is the standard approach for Faraday oscillations.[18] Our focus is the wetting properties defined by the static contact angle and the motion of the three-phase contact-line, which obeys a constitutive law that relates the contact-angle to the contact-line speed.

Lord Rayleigh[19] showed that free drops exhibit a discrete spectrum, which has come to be referred to as the Rayleigh–Lamb (RL) spectrum.[20] The RL spectrum has been verified experimentally for free drops[21,22] and is relevant in applications where the drop may not be completely free.[23,24] Typical extensions for free drops include, but are not limited to, the effects of (i) viscosity,[25–28] (ii) large-amplitude perturbations[29,30] or (iii) constrained geometries.[31–34] Recent experiments by Chang *et al.*[13] have shown the inadequacy of the RL spectrum for partially-wetting drops ($\alpha = 75°$) with pinned contact lines. The theory developed by Bostwick and Steen,[35] which accounts for wetting and spreading across a solid substrate, compares favorably with these experiments.

Forced drops exhibit a finite bandwidth of forcing frequencies over which a particular mode may be excited, in contrast to the discrete (delta-function) response for unforced drops. Chang *et al.*[36] observed frequency bands in experiments on mechanically-excited sessile water drops over a range of static contact angles. When bulk viscosity is included in our model, the governing equations can be recast in the form of a damped-driven oscillator with dissipation encompassing bulk dissipation from viscosity and contact-line dissipation related to the dynamic effects associated with the contact-line speed law, as outlined in Bostwick and Steen,[37] Section 3.3, who have termed this Davis dissipation since it can be traced back to the work of Davis[38] on fluid rivulets. Recent work has shown that energy can be generated for non-monotonic contact-line speed laws (*e.g.* Benilov and Billingham,[39] Appendix A). Note that we use a monotonic law in this paper to report modal dependence on wetting and first order effects of contact-line mobility, consistent with linear theory.

[a] *Department of Mechanical Engineering, Clemson University, Clemson, SC 29631, USA. E-mail: jbostwi@clemson.edu*

[b] *School of Chemical and Biomolecular Engineering and Center for Applied Mathematics, Cornell University, Ithaca, NY 14853, USA*

† Electronic supplementary information (ESI) available. See DOI: 10.1039/c6sm01928e

More complicated behaviors, such as loops and hysteresis observed in oscillatory contact-lines are outside the scope of this paper.[40,41]

Davis dissipation occurs for drops with finite contact-line mobility and leads to attenuated droplet response and increased bandwidth, even for inviscid fluids.[42,43] However, the scaling of Davis dissipation differs from that for bulk viscous effects. For reference, the decay rate γ from viscous dissipation for a free drop scales with the viscosity ν as $\gamma = \nu/R^2(k-1)(2k+1)$.[20] We compute the critical mobility and forcing frequency to generate the largest Davis dissipation in order to guide future experiments. With regard to comparison against the Chang *et al.*[36] experiments, we use the contact-line mobility as a fit parameter to account for the observed frequency envelopes.

Bulk dissipation from viscosity is approximated with the irrotational flow field. Viscosity tends to decrease the droplet amplitude response and increase the bandwidth for a given mode. Our bandwidth predictions compare favorably against experiment over a range of contact angles.[44] In addition, we compute the critical viscosity above which the oscillations for a particular mode become overdamped. This represents a bound above which a given mode cannot be harmonically excited.

Bosstwick and Steen[35] have shown that spectral ordering for the sessile drop can become broken and spectral lines mix for a range of contact angles. For the forced problem with finite bandwidth, we show that two distinct modes may be simultaneously excited by a single forcing frequency and map these regions of modal coexistence in parameter space for a number of modal pairs. Modal coexistence has been observed in oscillating liquid puddles and where it has been seen as a precursor to chaotic dynamics.[45] Identifying these regions is important for 3D printing,[1] mixing[46] and drop atomization[47] applications. The contact-line mobility strongly affects the size of the coexistence regions. Chang *et al.*[36] have shown that mode selection in experiment can be hysteretic in the coexistence regimes. Then the dominant mode depends upon the direction of the frequency sweep. Some modes also superpose linearly and exhibit no hysteresis. Here we focus on generating 'operating windows' for particular droplet behavior.

2 Mathematical formulation

Our derivation follows the boundary integral approach of Bostwick and Steen,[48] Section 1 in which normal modes are invoked and the flow problem (interior domain) is mapped onto the undisturbed interface.

Consider an incompressible, viscous fluid subject to a time-dependent pressure field $p(t) = P_0 e^{i\Omega t}$, occupying a domain D bounded by a spherical-cap interface ∂D^f held by a constant surface tension σ and a support surface ∂D^s, as shown in Fig. 1. The equilibrium surface Γ is defined parametrically,

$$\begin{aligned} X(s,\varphi;\alpha) &= \frac{\sin(s)}{\sin(\alpha)}\cos(\varphi),\ Y(s,\varphi;\alpha) = \frac{\sin(s)}{\sin(\alpha)}\sin(\varphi), \\ Z(s;\alpha) &= \frac{\cos(s)-\cos(\alpha)}{\sin(\alpha)}, \end{aligned} \tag{1}$$

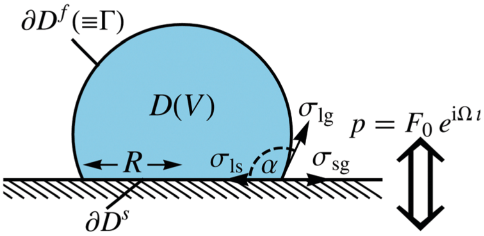

Fig. 1 Definition sketch: spherical-cap droplet of volume V and free surface Γ with contact angle α and liquid/gas σ_{lg}, solid/gas σ_{sg} and liquid/solid σ_{ls} surface tensions, driven by an applied pressure field $p = F_0 e^{i\Omega t}$ of amplitude F_0 and frequency Ω.

using arclength-like $s \in [0,\alpha]$ and azimuthal angle $\varphi \in [0,2\pi]$ as surface coordinates, with α the static contact-angle. The interface is given a small perturbation $\eta(s,\varphi,t)$. No domain perturbation is needed for small deformations, thus the droplet domain D is bounded by a free surface $\partial D^f(\equiv\Gamma)$ of constant surface tension σ, and a planar surface-of-support ∂D^s.

2.1 Governing hydrodynamic equations

We assume the velocity field $v = -\nabla\Psi$ can be expressed using the velocity potential Ψ,[49] noting that this form of the velocity field cannot satisfy the no-slip condition on the solid support, but we can evaluate the bulk dissipation from the irrotational field. The velocity potential Ψ satisfies the following boundary value problem,

$$\nabla^2\Psi = 0[D],\ \nabla\Psi\cdot\hat{z} = 0[\partial D^s],\ \frac{\partial\Psi}{\partial n} = -\frac{\partial\eta}{\partial t}[\partial D^f]. \tag{2}$$

The pressure field p is given by the linearized Bernoulli equation

$$p = \rho\frac{\partial\Psi}{\partial t} + P_0 e^{i\Omega t}[D], \tag{3}$$

where ρ is the fluid density. Finally, disturbances to the equilibrium surface Γ generate pressure gradients, and thereby flows, according to the Young–Laplace equation

$$p - \mu\hat{n}\cdot(\nabla\otimes\nabla\Psi)\cdot\hat{n} = -\sigma(\Delta_\Gamma\eta + (\kappa_1{}^2 + \kappa_2{}^2)\eta)[\partial D^f], \tag{4}$$

where $\otimes$ is the tensor product and μ the fluid viscosity. The Laplace–Beltrami operator Δ_Γ is defined on the equilibrium surface Γ and operates on functions η,

$$\Delta_\Gamma\eta \equiv \frac{1}{\sqrt{g}}\frac{\partial}{\partial u^\mu}\left(\sqrt{g}g^{\mu\nu}\frac{\partial\eta}{\partial u^\nu}\right) \tag{5}$$

with the surface metric given by

$$g_{\mu\nu} = \begin{pmatrix} \csc^2(\alpha) & 0 \\ 0 & (\csc(\alpha)\sin(s))^2 \end{pmatrix},\ g = \det(g_{\mu\nu}), \tag{6}$$

and $\mu, \nu = 1, 2$, using notation standard to differential geometry, *e.g.* Kreyszig.[50]

The governing eqn (2)–(4) are augmented with a boundary condition on the three-phase contact-line to yield a well-posed system of partial differential equations, a condition which we discuss later.

2.2 Normal mode reduction

We assume normal modes for the interface disturbance η and velocity potential Ψ,

$$\eta(s,\varphi,t) = y(s)e^{i\ell\varphi}e^{i\Omega t},\ \Psi(x,t) = \phi(r,\theta)e^{i\ell\varphi}e^{i\Omega t}, \tag{7}$$

with ℓ the azimuthal wavenumber and Ω the forcing frequency. Here (r,θ) are spherical coordinates. The normal stress balance at the interface (4) can be written as

$$\begin{aligned}&\left(\frac{\partial\phi}{\partial n}\right)'' + \cot(s)\left(\frac{\partial\phi}{\partial n}\right)' + \left(2 - \frac{\ell^2}{\sin^2(s)}\right)\left(\frac{\partial\phi}{\partial n}\right)\\ &\quad = \csc^2(\alpha)\left(\lambda^2\phi - i\lambda\varepsilon\hat{n}\cdot(\nabla\otimes\nabla\phi)\cdot\hat{n} + \lambda F_0\right),\end{aligned} \tag{8}$$

where $\varepsilon \equiv \mu/\sqrt{\rho R\sigma}$ is the Ohnesorge number, $\lambda \equiv \Omega\sqrt{\rho R^3/\sigma}$ the scaled forcing frequency, $F_0 = P_0R^2/\sigma$ the scaled forcing amplitude and $' = \mathrm{d}/\mathrm{d}s$. The contact-line dynamics obey the general contact-line law relating the linearized deviation in contact-angle from its static value $\Delta\alpha$ to the contact-line speed u_{CL}, $\Delta\alpha = \Lambda u_{CL}$ (*cf.* Fig. 2);

$$\frac{\partial}{\partial s}\left(\frac{\partial\phi}{\partial n}\right) + \cos(\alpha)\left(\frac{\partial\phi}{\partial n}\right) = i\lambda\Lambda\left(\frac{\partial\phi}{\partial n}\right), \tag{9}$$

where Λ is the contact-line mobility.[38,51] Note that $\Lambda = 0$ corresponds to the free and $\Lambda = \infty$ to the pinned contact-line disturbance, respectively. The velocity potential additionally satisfies the following auxiliary conditions,

$$\begin{aligned}&\nabla^2\phi - \frac{\ell^2}{r^2\sin^2\theta}\phi = 0[D],\ \frac{\partial\phi}{\partial n} = 0[\partial D^{\mathrm{s}}],\\ &\frac{\partial\phi}{\partial n} = -i\lambda y[\partial D^{\mathrm{f}}],\ \int_\Gamma \frac{\partial\phi}{\partial n}\mathrm{d}\Gamma = 0,\end{aligned} \tag{10}$$

with the Laplacian ∇^2 in (10) a function of (r,θ).

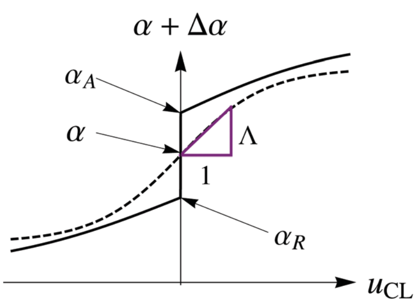

Fig. 2 Dynamic contact-line condition relates the contact angle to the contact-line speed u_{CL} with hysteresis (solid) and without (dashed). Here, α_a and α_r are the advancing and receding static contact angles ($u_{\mathrm{CL}} \to 0$), respectively. Limiting cases of the continuousï contact-line law (dashed) include the fixed contact-angle $\Lambda = 0$ and pinned contact-line $\Lambda = \infty$ conditions.

2.3 Solution of governing equations

We write the solution to (8)–(10) as an integral equation

$$\begin{aligned}\left(1-b^2\right)\frac{\partial\phi}{\partial n}(x) \;=\; & -i\lambda\varepsilon\int_b^1 G(x,y)(\hat{n}\cdot(\nabla\otimes\nabla\phi)\cdot\hat{n})\mathrm{d}y\\ & + \lambda^2\int_b^1 G(x,y)\phi(y)\mathrm{d}y + F_0\lambda\int_b^1 G(x,y)\mathrm{d}y,\end{aligned} \tag{11}$$

using the Green's function G defined in the Appendix. Here $x \equiv \cos(s)$, $b \equiv \cos(\alpha)$. Note that the Green's function is parameterized by azimuthal wavenumber ℓ, forcing frequency λ and contact-line mobility Λ.

A solution series

$$\phi = \sum_{j=1}^{N} a_j\phi_j, \tag{12}$$

is applied to (11) and inner products are taken to generate a set of algebraic equations

$$\sum_{j=1}^{N}\left(m_{ij} + i\varepsilon\lambda\tau_{ij} - \lambda^2\kappa_{ij}\right)a_j = F_0\lambda\gamma_i, \tag{13}$$

with

$$\begin{aligned}m_{ij} &\equiv \left(1-b^2\right)\int_b^1 \frac{\partial\phi_i}{\partial n}\phi_j\mathrm{d}x,\\ \kappa_{ij} &\equiv \int_b^1\int_b^1 G(x,t)\phi_i(t)\phi_j(x)\mathrm{d}x\mathrm{d}t\\ \tau_{ij} &\equiv \int_b^1\int_b^1 G(x,t)(\hat{n}\cdot(\nabla\otimes\nabla\phi_i)\cdot\hat{n})\phi_j(x)\mathrm{d}x\mathrm{d}t,\\ \gamma_i &\equiv \int_b^1\int_b^1 G(x,t)\phi_i(x)\mathrm{d}x\mathrm{d}t.\end{aligned} \tag{14}$$

The auxiliary conditions (10) are satisfied through proper selection of the basis functions ϕ_j, as discussed in Bostwick and Steen,[35] Section 4.2. For zonal ($\ell = 0$) modes,

$$\phi_j(\rho,\theta) = \rho^{2j}P_{2j}(\cos\theta), \tag{15}$$

while for non-zonal ($\ell \neq 0$) modes,

$$\phi_j^{(\ell)}(\rho,\theta) = \rho^{j}P_j^{(\ell)}(\cos\theta) \tag{16}$$

with $j + \ell$ = even.

3 Results

For fixed λ, ε, α, ℓ, we compute the solution vector a_j to the matrix eqn (13). The associated fluid response ϕ, $\partial\phi/\partial n$ is then obtained by applying a_j to (12). Modal identities are distinguished by the wavenumber pair $[k,\ell]$ that follow the spherical harmonic classification scheme; zonal $[k,0]$, sectoral $[k,k]$ and tesseral $[k,\ell \neq k]$ shapes, as shown in Fig. 3. An alternate identification uses layers and sectors.[36] The focus here is the droplet response a_j, which is linear in the applied pressure amplitude F_0. Henceforth, we

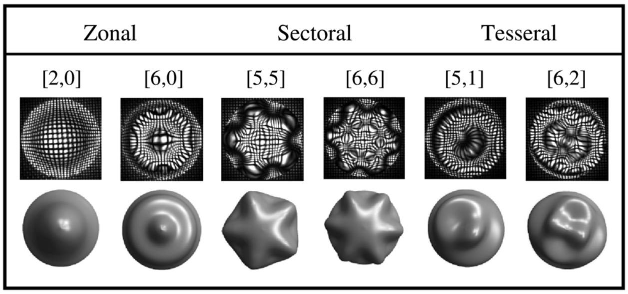

Fig. 3 Modal classification by wavenumber pair $[k,\ell]$ into zonal $[k,0]$, sectoral $[k,k]$ and tesseral $[k,\ell \neq k]$ shapes. Experimental images are reproduced from Chang *et al.*[36]

report the complex response as the vector $c_j \equiv a_j/F_0$, which admits a phase shift

$$\delta = \arctan\left|\frac{\mathrm{Im}[c]}{\mathrm{Re}[c]}\right|. \tag{17}$$

For $\delta = 0°$ and $\delta = 90°$, the droplet response is in-phase and out-of-phase with the applied pressure oscillations, respectively, with $\delta = 90°$ corresponding to a state of maximal dissipation. Note the damped-driven oscillator structure of (13) with corresponding features. In what follows, we show how the response diagram changes with contact-line mobility Λ and viscosity ε, comprehensively explore the parameter space, and compare against relevant experiments when appropriate.

3.1 CL mobility Λ

We examine the role of contact-line mobility by plotting the response diagram and phase shift for the zonal $\ell = 0$ modes for an inviscid $\varepsilon = 0$ drop with $\alpha = 75°$ in Fig. 4 for various values of Λ. We set $\varepsilon = 0$ to eliminate the effects of bulk viscous dissipation. For fully-mobile $\Lambda = 0$ and pinned $\Lambda = \infty$ disturbances, the respective resonance peaks are infinite and the droplet oscillates in phase $\delta = 0°$ with the forcing frequency. However, for finite values of Λ the resonance peak becomes finite and the oscillations become out-of-phase with the driving field, indicating that finite contact-line mobility Λ leads to an effective dissipation.

At the mobility Λ_m, the resonance peak will be smallest and the droplet response is minimal. We call Λ_m the critical mobility and λ_m the critical frequency that generates the largest Davis dissipation. Fig. 5 plots Λ_m, λ_m against contact-angle α for the $k = 1$–4 modes. The forcing frequency λ_m monotonically decreases with increasing contact angle, while the mobility Λ_m is more complex. For example, the zonal modes [2,0], [4,0] can have the smallest or largest critical mobility, for fixed polar wavenumber k, depending upon the contact angle. An important aspect of this study is the damping of oscillations for inviscid ($\varepsilon = 0$) fluids. Fig. 5 may be interpreted as a guide in selecting substrates for experiments that generate the largest Davis dissipation.

The response diagrams of Fig. 4 and 7, show that modes can be excited over a range of forcing frequencies. This has been observed in recent experiments for a number of modes and over a range of contact angles.[36] In that study, predicted frequency envelopes for pinned ($\Lambda = \infty$) disturbances with $\varepsilon = 0.0024$

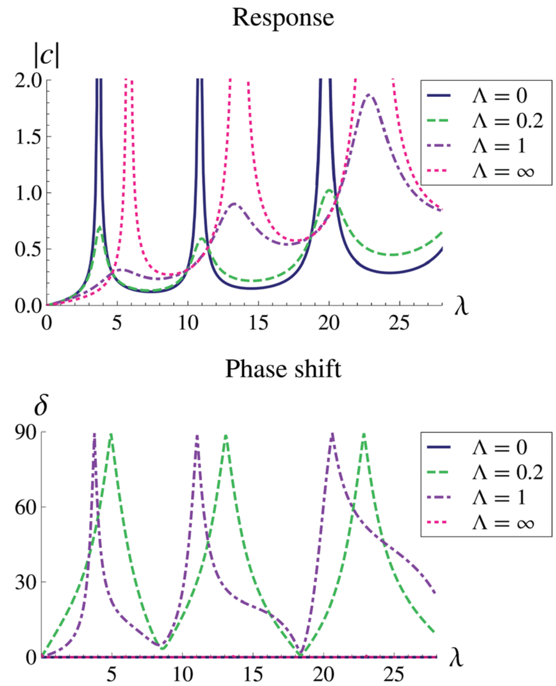

Fig. 4 Response $|c|$ (top) and phase shift δ (bottom) against frequency λ for the zonal $\ell = 0$ modes of an inviscid $\varepsilon = 0$ drop with $\alpha = 75°$, as it depends upon the mobility Λ. The first peak corresponds to the [2,0] mode, the second to [4,0] and the third to [6,0]. Note that the response is strictly real with phase shift $\delta = 0°$ for the free $\Lambda = 0$ and pinned $\Lambda = \infty$ disturbances (superposed lines on λ axis). For finite mobility Λ, the drop response is out-of-phase $\delta = 90°$ at the resonant peak.

compared favorably to experiment for a large number of modes, with the exception of the [5,5], [7,7], [9,9] sectoral modes. By using the contact-line mobility as a fit parameter $\Lambda = 0.1$, we find frequency envelopes that match the experiments for those remaining modes, suggesting that the contact-line dynamics may be crucial in understanding the forced oscillations problem (*cf.* Fig. 6).

3.2 Viscosity ε

Fig. 7 plots the droplet response and phase shift for the zonal modes for a sub-hemispherical drop ($\alpha = 75°$) with $\Lambda = 0$, as they depend upon the bulk viscosity ε. For an inviscid fluid $\varepsilon = 0$, the oscillations are completely in phase $\delta = 0°$ with the applied field and the response diagram exhibits three infinite peaks that correspond to the [2,0], [4,0] and [6,0] modes, respectively. Note that modes appear over a range of frequencies that define a bandwidth, a prominent feature of the forced oscillation problem that is also observed in experiment.[36] For small viscosity $\varepsilon = 0.01$, the resonance peaks are dramatically lowered and the droplet response is out of phase $\delta \neq 0°$ with the driving frequency. The relative decrease in response amplitude $|c|$ for increasing wavenumber is consistent with bulk viscous effects $\varepsilon \neq 0$ from traditional viscous dissipation.[20] For finite viscosity $\varepsilon \neq 0$ and contact-line mobility $\Lambda \neq 0, \infty$, the response can be non-monotonic because of competition between bulk and Davis dissipation. No systematic trend is observed in these regimes.

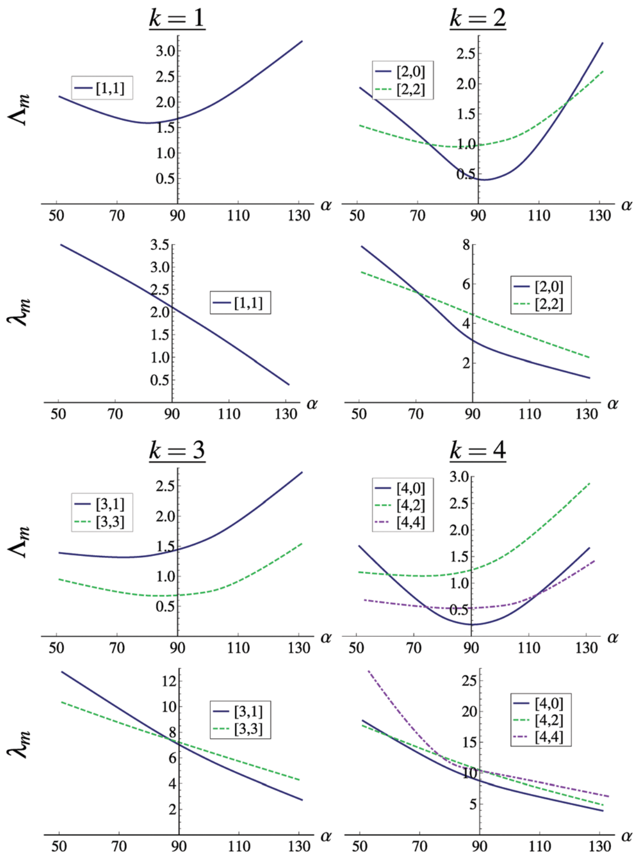

Fig. 5 Critical mobility Λ_m and critical frequency λ_m that generates the largest Davis dissipation for fixed polar wavenumber k, as it depends upon the contact-angle α and azimuthal wavenumber ℓ. Viscous effects are negligible $\varepsilon = 0$. Note the different vertical scales between sub-figures.

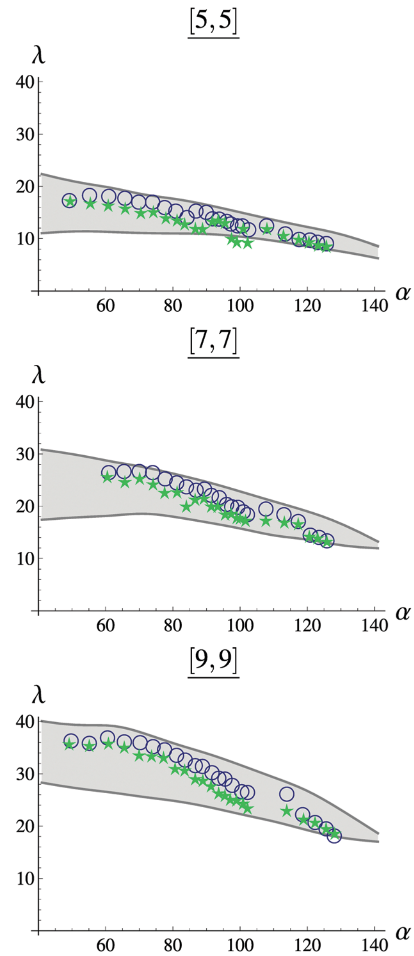

Fig. 6 Comparison with Chang *et al.*[36] experiments: frequency envelopes against contact-angle α for sectoral modes [5,5], [7,7], [9,9] with contact-line mobility $\Lambda = 0.1$ (fit to experiment) and $\varepsilon = 0.0024$ (measured in experiment). Experiments given by symbols.

Resonance peaks may disappear completely for large values of viscosity, as shown in Fig. 7 for the [4,0] and [6,0] modes with $\varepsilon = 0.5$. For a given mode $[k,\ell]$, one can define a critical Ohnesorge number ε_c where the resonance peak disappears and above which ($\varepsilon > \varepsilon_c$) it is not possible to excite that mode. Stated differently, beyond ε_c the oscillations are over-damped. Fig. 8 plots ε_c against contact angle for the pinned $\Lambda = \infty$ modes. Note that for a fixed azimuthal wavenumber ℓ, ε_c decreases with increasing polar wavenumber k irrespective of contact-angle, as could be expected from the increased surface distortion for the high wavenumber modes (Chang *et al.*,[36] Fig. 7). However, the non-monotonic behavior with contact angle α could not have been predicted *a priori* and presumably results from the interactions between adjacent modes and the applied pressure field.

A typical measure of the damping of oscillations in forced systems is the bandwidth of a resonance peak, which can easily be extracted from the response diagram (*e.g.* Fig. 7). In particular, the full width at half max (FWHM) bandwidth also coincides with the decay rate of oscillations.[44] Fig. 9(a) plots the dimensionless FWHM $\Delta\lambda$ against ε and α for the [1,1] pinned mode. Note the non-monotonic dependence of the dissipation (FWHM) with respect to contact angle, reflecting the increased presence of the solid substrate for these wetting conditions. We compare our FWHM bandwidth predictions $\Delta\Omega$ for the [1,1] pinned mode to the experiments by Sharp[44] over a wide range of contact angles in Fig. 9(b). The agreement is reasonable over a large range of drop volumes, as measured by the drop mass m.

3.3 Modal coexistence

An important prediction from Bostwick and Steen[35] was that two modes with different wavenumber pair $[k,\ell]$ may share the same natural frequency and that the classical ordering of frequencies by increasing polar wavenumber could become broken and unordered for certain contact angles. This was confirmed in the experiments by Chang *et al.*[36]

A primary difference between natural and forced oscillations is that the resonance frequency takes a discrete value for the former and a range of values for the latter. Hence, two modes may coexist over a range of frequencies for the forced problem considered here. Fig. 10(a) plots the frequency envelopes for the pinned [6,0] zonal and [5,5] sectoral modes against contact angle α for the Ohnesorge number $\varepsilon = 0.0024$ used in the Chang *et al.*[36] experiments. Modal coexistence is predicted in the region shown in Fig. 10(b). In general, the domains of coexistence for a pair of

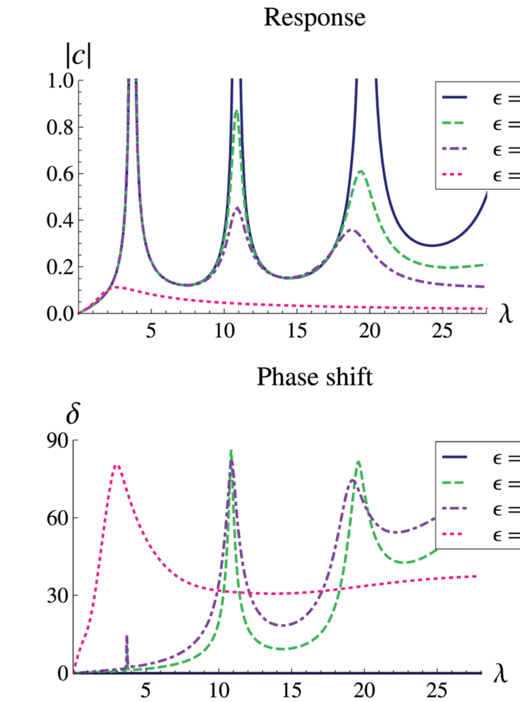

Fig. 7 Response $|c|$ (top) and phase shift δ (bottom) against frequency λ for a drop with $\alpha = 75°$, $\Lambda = 0$ (fully-mobile disturbance) and $\ell = 0$, as it depends upon the Ohnesorge number ε. The first peak corresponds to the [2,0] mode, the second to [4,0] and the third to [6,0]. Note for inviscid fluids $\varepsilon = 0$, the phase shift $\delta = 0°$ for all α.

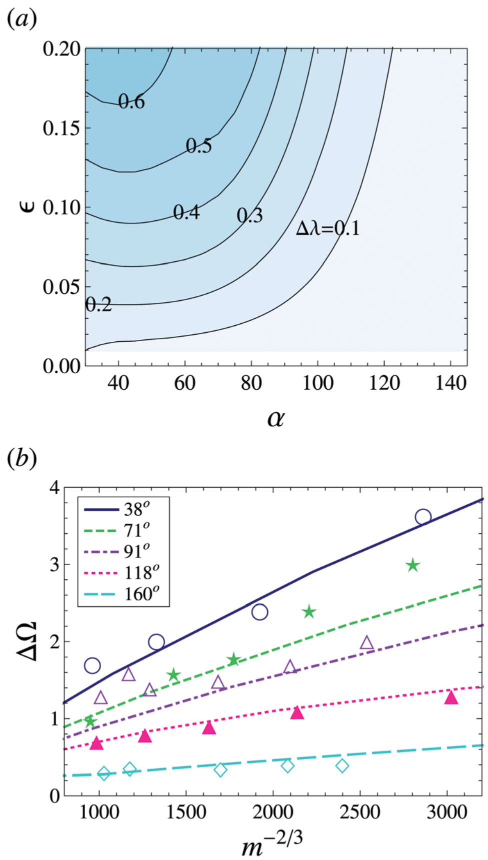

Fig. 9 Full width at half max (FWHM) for the [1,1] pinned mode: (a) dimensionless frequency $\Delta\lambda$ against Ohnesorge number ε and contact-angle α and (b) dimensional frequency $\Delta\Omega$ against $1/m^{2/3}$ for 10 w% glycerol droplets comparing to Sharp[44] (symbols).

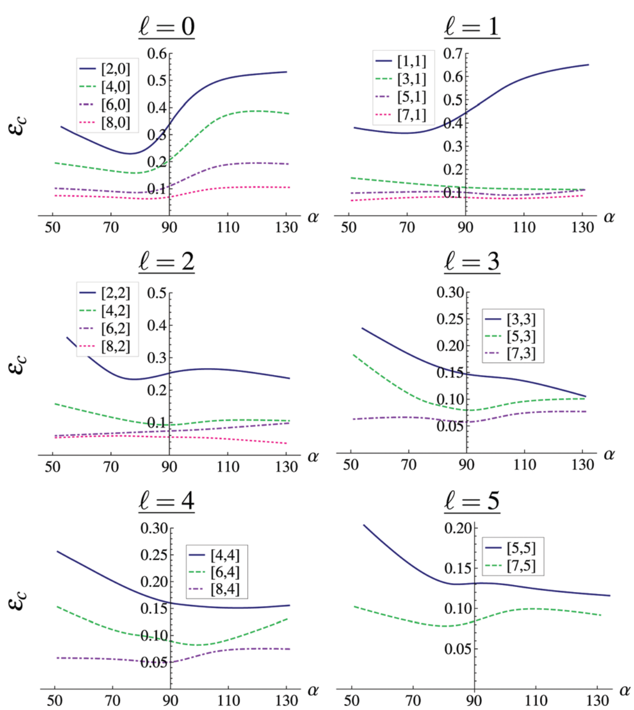

Fig. 8 Critical Ohnesorge number ε_c against contact-angle α for pinned disturbances $\Lambda = \infty$. Mode $[k,\ell]$ can be excited below the corresponding curve. Note the different vertical scales between sub-figures.

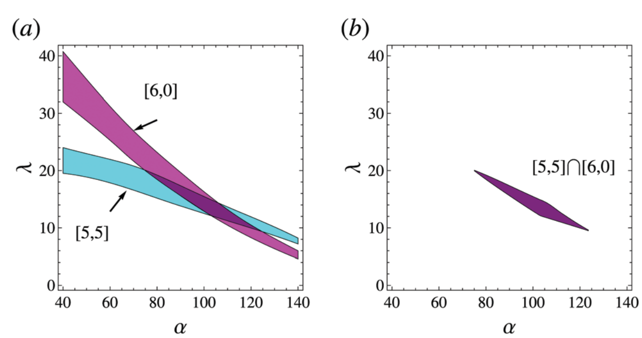

Fig. 10 Modal coexistence: (a) frequency λ envelopes for the pinned ($\Lambda = \infty$) [6,0] and [5,5] modes against contact-angle α predicts (b) domains of coexistence for a drop with $\varepsilon = 0.0024$.

modes will depend upon both the contact-line mobility Λ and the Ohnesorge number ε. Fig. 11 plots the domains of coexistence for a given zonal mode with the sectoral modes, comparing pinned $\Lambda = \infty$ disturbances to those with finite mobility $\Lambda = 0.1$. As shown, decreasing Λ tends to increase the number of modes that coexist with a given target mode. For reference, we include additional figures that predict domains of coexistence for different target modes in the ESI.†

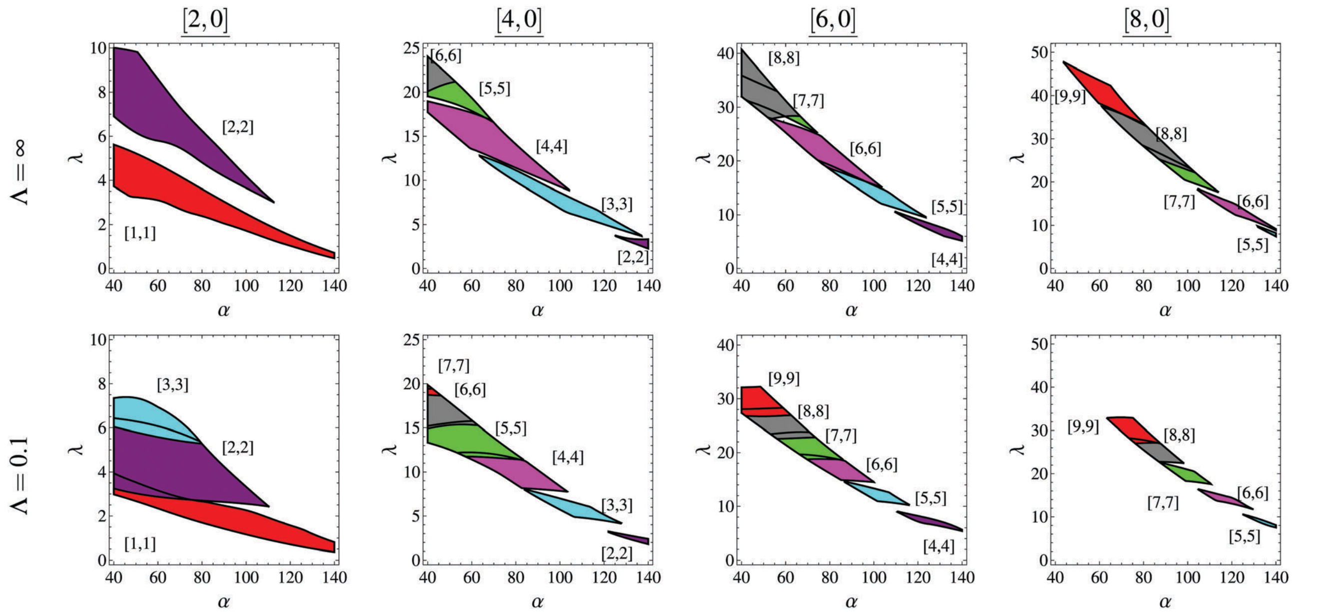

Fig. 11 Domains of coexistence for the zonal modes $[k,0]$ mixed with the sectoral modes $[k,k]$ for pinned $\Lambda = \infty$ and finite contact-line mobility $\Lambda = 0.1$ disturbances with $\varepsilon = 0.0024$. Note the different frequency scales between sub-figures.

4 Concluding remarks

We have studied the forced oscillations of a partially-wetting sessile drop, whose three-phase contact line obeys a constitutive law relating the contact angle to the contact line speed, sometimes called the Hocking condition. Response diagrams and phase shifts are reported, as they depend upon viscosity ε and contact line mobility Λ. Modes are distinguished by the wavenumber pair $[k,\ell]$ and can be excited over a range of frequencies that define a bandwidth. Our predictions compare well against relevant experiments on vibrated sessile drops (*cf.* Fig. 6 and 9(b)).

Our focus is on defining regimes or 'operating windows' where certain droplet behavior may be observed experimentally or our model developed further. For example, we compute the critical viscosity ε_c (Ohnesorge number) above which it is not possible to observe a specified mode over a range of contact angles, thereby aiding the practitioner in selecting appropriate fluids and droplet volumes (*cf.* Fig. 8). We then show how finite contact line mobility Λ leads to Davis dissipation, even in inviscid fluids, and compute the critical mobility Λ_m and forcing frequency λ_m that generate the largest dissipation (*cf.* Fig. 5). Finally, we show that two distinct modes may be simultaneously excited by a single forcing frequency and map these regions of modal coexistence in parameter space for a number of modal pairs in Fig. 11. Modal coexistence may be of importance in mixing applications that rely upon capillary oscillations[46,52,53] and drop atomization[12,47] for spray cooling. With regard to modeling, a thorough study of the internal resonances and nonlinear modal interactions[54,55] in the coexistence domains would help identify the mechanism behind mode selection in related experiments.[36] Extensions to this study could include modeling (i) an asymmetric applied pressure field that could potentially lead to a translational droplet motion along the substrate[39,56] and (ii) a fully non-linear theory with associated contact-line law for oscillatory flows that exhibits effects such as hysteresis and loops.[40,41]

Appendix A

Green's function

The Green's function is defined as

$$G = \begin{cases} \xi(\ell)y_1(y;\ell)\left[\dfrac{\tau_2}{\tau_1}y_1(x;\ell) - y_2(x;\ell)\right] & b < x < y < 1 \\ \xi(\ell)y_1(x;\ell)\left[\dfrac{\tau_2}{\tau_1}y_1(y;\ell) - y_2(y;\ell)\right] & b < y < x < 1, \end{cases} \tag{18}$$

where $x \equiv \cos(s)$, $b \equiv \cos(\alpha)$. The functions y_1 and y_2 belong to the kernel of the curvature operator and are given by

$$y_1(x;0) = P_1(x),\ y_2(x;0) = Q_1(x),\ y_1(x;1) = P_1^{(1)}(x),$$

$$y_2(x;1) = Q_1^{(1)}(x),\ y_1(x;\ell \geq 2) = (x+\ell)\left(\frac{1-x}{1+x}\right)^{\ell/2},$$

$$y_2(x;\ell \geq 2) = \frac{(x+\ell)}{2\ell(\ell^2-1)}\left(\frac{1+x}{1-x}\right)^{\ell/2}, \tag{19}$$

where P_1, Q_1 and $P_1^{(1)}$, $Q_1^{(1)}$ are the order 0 and 1 Legendre functions of index 1, respectively.[57] Similarly, the scale factor is given by

$$\xi(\ell) \equiv \begin{cases} 1/2 & \ell = 1 \\ 1 & \ell \neq 1, \end{cases} \tag{20}$$

while

$$\begin{aligned}\tau_1 &= y_1{}'(b;\ell) + \left(\frac{b}{\sqrt{1-b^2}} - i\lambda\Lambda\right)y_1(b;\ell),\\ \tau_2 &= y_2{}'(b;\ell) + \left(\frac{b}{\sqrt{1-b^2}} - i\lambda\Lambda\right)y_2(b;\ell).\end{aligned} \quad (21)$$

Acknowledgements

PHS acknowledges support by NASA Grant NNX09AI83G and NSF Grant CBET-1236582.

References

1 P. Calvert, *Chem. Mater.*, 2001, **13**, 3299–3305.
2 T. Grimm, *User's Guide to Rapid Prototyping*, Society of Manufacturing Engineers, 2004.
3 Y. Park, H. Im, M. Im and Y. Choi, *J. Mater. Chem.*, 2011, **21**, 633–636.
4 H. Stone, A. Stroock and A. Ajdari, *Annu. Rev. Fluid Mech.*, 2004, **36**, 381–411.
5 J. R. Castrejon-Pita, W. R. S. Baxter, J. Morgan, S. Temple, G. D. Martin and I. M. Hutchings, *Atomization Sprays*, 2013, **23**, 541–565.
6 O. A. Basaran, H. Gao and P. P. Bhat, *Annu. Rev. Fluid Mech.*, 2013, **45**, 85–113.
7 J. Kim, *Int. J. Heat Fluid Flow*, 2007, **28**, 753–767.
8 T. D. Donnelly, J. Hogan, A. Mugler, N. Schommer, M. Schubmehl, A. J. Bernoff and B. Forrest, *Phys. Fluids*, 2004, **16**, 2843–2851.
9 D. Mampallil, H. B. Eral, A. Staicu, F. Mugele and D. van den Ende, *Phys. Rev. E: Stat., Nonlinear, Soft Matter Phys.*, 2013, **88**, 053015.
10 M. Baudoin, P. Brunet, O. Bou Matar and E. Herth, *Appl. Phys. Lett.*, 2012, **100**, 154102.
11 P. Deepu, S. Basu and R. Kumar, *Chem. Eng. Sci.*, 2014, **114**, 85–93.
12 B. Vukasinovic, M. Smith and A. Glezer, *J. Fluid Mech.*, 2007, **587**, 395–423.
13 C. Chang, J. Bostwick, P. Steen and S. Daniel, *Phys. Rev. E: Stat., Nonlinear, Soft Matter Phys.*, 2013, **88**, 023015.
14 C. F. Tilger, J. D. Olles and A. H. Hirsa, *Appl. Phys. Lett.*, 2013, **103**, 264105.
15 X. Noblin, A. Buguin and F. Brochard-Wyart, *Eur. Phys. J. E: Soft Matter Biol. Phys.*, 2004, **14**, 395–404.
16 P. Brunet, J. Eggers and R. Deegan, *Phys. Rev. Lett.*, 2007, **99**, 144501.
17 X. Noblin, R. Kofman and F. Celestini, *Phys. Rev. Lett.*, 2009, **102**, 194504.
18 T. B. Benjamin and F. Ursell, *Proc. R. Soc. London, Ser. A*, 1954, **225**, 505–515.
19 L. Rayleigh, *Proc. R. Soc. London*, 1879, **29**, 71–97.
20 H. Lamb, *Hydrodynamics*, Cambridge University Press, Cambridge, 1932.
21 E. Trinh and T. Wang, *J. Fluid Mech.*, 1982, **122**, 315–338.
22 T. Wang, A. Anilkumar and C. Lee, *J. Fluid Mech.*, 1996, **308**, 1–14.
23 X. Noblin, A. Buguin and F. Brochard-Wyart, *Phys. Rev. Lett.*, 2005, **94**, 166102.
24 N. A. Chebel, F. Risso and O. Masbernat, *Phys. Fluids*, 2011, **23**, 102104.
25 W. Reid, *Q. Appl. Math.*, 1960, **18**, 86–89.
26 S. Chandrasekhar, *Hydrodynamic and Hydromagnetic Stability*, Oxford University Press, Oxford, 1961.
27 C. Miller and L. Scriven, *J. Fluid Mech.*, 1968, **32**, 417–435.
28 A. Prosperetti, *J. Mec.*, 1980, **19**, 149–182.
29 J. Tsamopoulos and R. Brown, *J. Fluid Mech.*, 1983, **127**, 519–537.
30 T. Lundgren and N. Mansour, *J. Fluid Mech.*, 1988, **194**, 479–510.
31 M. Strani and F. Sabetta, *J. Fluid Mech.*, 1984, **141**, 233.
32 J. Bostwick and P. Steen, *Phys. Fluids*, 2009, **21**, 032108.
33 S. Ramalingam and O. Basaran, *Phys. Fluids*, 2010, **22**, 112111.
34 J. Bostwick and P. Steen, *J. Fluid Mech.*, 2013, **714**, 312–335.
35 J. Bostwick and P. Steen, *J. Fluid Mech.*, 2014, **760**, 5–38.
36 C. Chang, J. Bostwick, S. Daniel and P. Steen, *J. Fluid Mech.*, 2015, **768**, 442–467.
37 J. Bostwick and P. Steen, *Annu. Rev. Fluid Mech.*, 2015, **47**, 539–568.
38 S. Davis, *J. Fluid Mech.*, 1980, **98**, 225–242.
39 E. Benilov and J. Billingham, *J. Fluid Mech.*, 2011, **674**, 93–119.
40 C.-L. Ting and M. Perlin, *J. Fluid Mech.*, 1995, **295**, 263–300.
41 L. Jiang, M. Perlin and W. W. Schultz, *Phys. Fluids*, 2004, **16**, 748–758.
42 D. Lyubimov, T. Lyubimova and S. Shklyaev, *Fluid Dyn.*, 2004, **39**, 851.
43 D. Lyubimov, T. Lyubimova and S. Shklyaev, *Phys. Fluids*, 2006, **18**, 012101.
44 J. Sharp, *Soft Matter*, 2012, **8**, 399–407.
45 P. Brunet and J. H. Snoeijer, *Eur. Phys. J.: Spec. Top.*, 2011, **192**, 207–226.
46 D. Mampallil, D. van den Ende and F. Mugele, *Appl. Phys. Lett.*, 2011, **99**, 154102.
47 S. C. Tsai, S. K. Lin, R. W. Mao and C. S. Tsai, *Phys. Rev. Lett.*, 2012, **108**, 154501.
48 J. Bostwick and P. Steen, *J. Fluid Mech.*, 2013, **714**, 336–360.
49 J. Padrino, T. Funada and D. Joseph, *Int. J. Multiphase Flow*, 2007, **34**, 61–75.
50 E. Kreyszig, *Differential Geometry*, Dover Publications, New York, NY, 1991.
51 L. Hocking, *J. Fluid Mech.*, 1987, **179**, 253–266.
52 F. Mugele, J.-C. Baret and D. Steinhauser, *Appl. Phys. Lett.*, 2006, **88**, 204106.
53 L. Davoust, Y. Fouillet, R. Malk and J. Theisen, *Biomicrofluidics*, 2013, **7**, 044104.
54 R. Natarajan and R. A. Brown, *J. Fluid Mech.*, 1987, **183**, 95–121.
55 D. M. Henderson and J. W. Miles, *J. Fluid Mech.*, 1991, **222**, 449–470.
56 E. S. Benilov and C. P. Cummins, *Phys. Rev. E: Stat., Nonlinear, Soft Matter Phys.*, 2013, **88**, 023013.
57 T. MacRobert, *Spherical Harmonics*, Pergamon, New York, NY, 1967.